CrossMark

TECHNICAL PAPER

Numerical and experimental studies of phase difference effects on flow rate of peristaltic micro-pumps with pumping chambers in series configurations

Tzong-Shyng Leu[1] · **Ding-Cong Gong**[1] · **Dartzi Pan**[1]

Abstract This paper studies phase difference effects on the flow rate of peristaltic micro-pumps using numerical and experimental approaches. In numerical simulation, commercial software (CFD-ACE+) is used. To focus on the phase relationship of peristaltic micro-pumps, all geometric parameters of the pump are fixed for a baseline design and the diaphragm motion is assumed as a sinusoidal waveform with a fixed frequency of 1 Hz. The phase difference between neighboring chambers is varied from 30°–120° in 10° increments. The pump configurations include the basic 3-chamber configuration and the configurations with up to 8 chambers in series arrangements. The computational results indicate that the maximum flow rate Q_{max} increases with increasing number of chambers (n). However, the maximum phase difference $\Delta\phi_{max}$ for the maximum pump flow decreases with increasing number of chambers (n) in series pumps. The diaphragm oscillation amplitude also has a significant impact on the pumping flow rate. In the meantime, experiments are performed in an attempt to validate the computational findings. The pump diaphragm is fabricated using PDMS with iron particle contents, and permanent magnets are employed to actuate the diaphragm into movement. The phase relation between diaphragms are controlled by a set of rotary cams specially designed and fabricated for the experiments. Near rectangular waveform is used in the actuation of diaphragm movement. Results show that despite of the difference between computations and experiments, the basic trends

of increasing Q_{max} and decreasing $\Delta\phi_{max}$ with increasing number of chambers (n) are verified for peristaltic micro-pumps in series configurations.

1 Introduction

In recent years, microsystem technology has made great progresses and is applied to many fields such as biology, biomedical engineering, biochemistry research, etc. Microsystem applications in bio-related fields involve micro-fluidics components, such as micro-pumps, micro-valves, micro-channels, micro mixers and micro reactors. Generally, a micro-pump is used to drive the fluid in micro-channels; a micro-valve is used to control the direction of the flow; a micro mixer mixes fluids efficiently; a micro reactor is the device at which the designed reaction takes place. Finally, all these micro-fluidics components are connected by micro-channels and integrated into a microsystem with specific functions. When such microsystems are implemented on a microchip such that the chip can perform a specific task or procedure in the laboratory, the chip is called a Micro-Total-Analysis-System (μTAS) or a Lab-on-a-Chip.

Micro-pump is the heart of a micro-fluidics system because it is the power source to drive the fluid flow. A highly-integrated and self-contained active micro-pump is essential to a successful μTAS chip. According to the review papers (Shoji and Esashi 1994; Nguyen et al. 2002; Laser and Santiago 2004), most micro-pumps today can be roughly categorized into two groups: mechanical pumps with moving parts and non-mechanical pumps without moving parts. The mechanical pumps perform pressure work on the working fluid of the system via the moving boundary of reciprocating piston or oscillating diaphragm

✉ Tzong-Shyng Leu
tsleu@mail.ncku.edu.tw

[1] Department of Aeronautics and Astronautics, National Cheng Kung University, No. 1, University Road, Tainan 701, Taiwan, ROC

in the pumping chamber. Active check valves at the inlet and outlet of the pumping chamber are employed to control the direction of the pump flow. The non-mechanical pumps add energy continuously and directly to the working fluid by the interaction between the working fluid and the imposed fields, such as electromagnetic field, centrifugal force field, or ultra-sonic wave field. There is a sub-category in mechanical micro-pumps called peristaltic micro-pumps that have three or more pumping chambers operating in a special peristaltic actuation sequence to drive the working fluid. Unlike the mechanical pumps with active check valves, peristaltic micro-pumps control the direction of the pump flow by varying the actuation sequence of the pumping chamber. Perhaps the first peristaltic micro-pump is developed by Smits (1990) using three pumping chambers driven by piezoelectric actuators operating in a 6-step peristaltic sequence to pump the working fluid in the micro-channel.

The main advantage of a peristaltic micro-pump is its simplicity in design and fabrication. The pumping chamber has no moving parts other than the pumping diaphragm, and all three pumping chambers are identical. This is relatively simple as compared to a regular mechanical micro-pump with active check valves. The pump flow can be bi-directional, depending on the peristaltic sequence adopted in the operation. The main disadvantages of such a peristaltic micro-pump are that each pumping chamber will have to be operated and controlled independently and that the pumping efficiency is relatively low because of the fact that no check valve is employed.

There has been many research and development on peristaltic micro-pumps since Smits' (1990) works. Generally, the actuation principle of peristaltic pumps can be piezoelectric (Smits 1990; Jang et al. 2007; Li et al. 2007), electrostatic (Xie et al. 2004; Lin et al. 2007; Lotz et al. 2009), thermo-pneumatic (Grosjean and Tai 1999; Boden et al. 2008; Yang and Liao 2009), pneumatic (Wang and Lee 2006; Wu et al. 2008; Huang et al. 2008), piston-type (Oh et al. 2005; Pilarski et al. 2005; Trenkle et al. 2009), rotary (Kim et al. 2002; Du et al. 2009; Koch et al. 2009), magnetic (Pan et al. 2004; Shen and Gijs 2009; Shen et al. 2011) and more. The actuation principle employed in the design of peristaltic pumps basically determines the energy source and the mechanism to convert the energy input into the movement and displacement of the diaphragm of the pumping chamber. The peristaltic motion of the fluid flow can be generated by operating the pumping chambers in a chosen peristaltic order of 6-step, 5-step, 4-step and 3-step operation. The chosen peristaltic working sequence is the most important factor in determining the direction and the magnitude of the net pump flow. Many other geometrical parameters also affect the pump flow. For example, the size and shape of the pumping chamber, and its diaphragm, the

cross-sectional area and length of the micro-channels in the system, and the system configuration of pumping chambers, etc.

To complete one cycle of peristaltic sequence of chamber operation requires one period (T) of the peristaltic sequence. The net fluid volume (ΔV) being moved from the inlet to the outlet of the pump in one complete period of the peristaltic sequence gives the net pump volume flow. When one defines the frequency (f) of the working peristaltic sequence, the net pump volume flow is not always linearly proportional to the working frequency (Xie et al. 2004). The period (T) or the frequency (f) all depend on the operation conditions such as the response time of the pumping diaphragm, the actuation time of each pumping chamber, the flow conditions at the inlet and the outlet of the pump, etc., the linearity between pump flow rate and the operation frequency is valid in a relatively low frequency range and there is a upper limit on the maximum pump flow one can get by increasing the working frequency. Nonetheless, it is an effective way to increase the pump flow rate of a peristaltic micro-pump when it is operated in the linear range.

The other way to increase the micro-pump flow rate is to increase the net volume (ΔV) being driven through in one period of peristaltic sequence. The major factors affecting ΔV are: the stroke volume (V_{stroke}) of a pumping chamber, the number of pumping chambers in the system and how they are configured relative to each other, and the phase difference between the operations of individual chambers. The stroke volume is defined as the volume swept by the pumping diaphragm in one cycle of diaphragm movement. Figure 1 defines the stroke volume of a 2D diaphragm movement. The stroke volume is equivalent to the volume difference between the maximum chamber volume and the minimum chamber volume as pumping diaphragm expands and compresses in the chamber. This volume obviously increases with increasing diaphragm displacement amplitude. The chamber volume that has not been swept by the diaphragm is the dead volume of the pumping chamber.
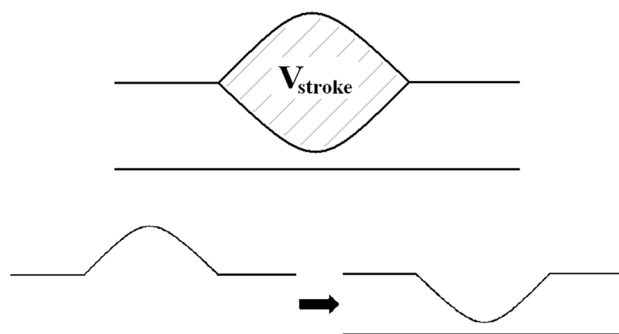

Fig. 1 Schematic of stoke volume generated by 2D diaphragm movement from open position to close position

Generally, increasing the diaphragm displacement amplitude is an effect way to increase the stroke volume (ΔV_{stroke}). However since it takes time for the diaphragm to complete its displacement cycle, the increase in the amplitude also increases the response time of the diaphragm, and one must assess its impact on the period (T) of the peristaltic sequence.

When active check valves are used in a mechanical pump, the pump diaphragm movement will drive one complete stroke volume moving in the controlled flow direction. For the peristaltic micropump designed by Smits (1990), the leftmost and the rightmost pumping chambers act like the check valve at the inlet and the outlet of the center pumping chamber. Thus although there are three pumping chambers, but only the stroke volume of the center chamber is transformed into pump flow in this peristaltic sequence. The pumping efficiency is obviously less than that of pump with active check valves. This is common in peristaltic micro-pumps, because no check valve is explicitly employed in pump design, and the direction-control function of check valve must be performed by the phase difference between the actuation of individual pumping chamber.

Another way to increase the total stroke volume is to increase the number of the pumping chambers in the pump, since the total stroke volume is linearly proportional to the number of pumping chambers. One can adopt a series configuration as in Fig. 2a. The immediate question that follows is that what is the best peristaltic sequence for these configurations? According to studies by Yang and Liao (2009), peristaltic micropumps of 3, 5 and 7 chambers in series configurations are studied mainly for the frequency effect on flow rate under ad-hoc peristaltic sequence. No phase difference effect has been studied in their work.

2 Numerical simulation and experimental methods

In this paper, peristaltic operations are studied using computational fluid dynamics (CFD) techniques with experimental validation to investigate the peristaltic micro-pumps.

2.1 Numerical simulation

In numerical simulation approach, computational fluid dynamics (CFD) commercial software is used to comprehensively investigate the flow flied of peristaltic micro-pumps. The software is CFD-ACE+ (version: 2003) developed by CFD Research Corporation (CFDRC) to perform numerical experiments on peristaltic micro-pumps. The governing equations relevant to this research are the laminar, incompressible continuity and Navier-stoke equations:

$$\vec{\nabla} \cdot \vec{V} = 0 \tag{2a}$$

$$\frac{\partial \vec{V}}{\partial t} + \vec{\nabla} \cdot \left(\vec{V}\vec{V} \right) = -\frac{1}{\rho} \vec{\nabla} P + \frac{1}{Re} \nabla^2 \vec{V} \tag{2b}$$

where $\vec{V}$ is velocity; ρ is density; P is pressure; Re is Reynolds number. Here, all variables are non-dimensionalized by proper reference values. CFD-ACE+ employs a cell-centered finite volume method to solve the Navier–Stokes equations. All variables, including velocity and pressure, are stored at the cell centers of the grid mesh. It uses the SIMPLEC solution method (semi-implicit method for pressure-linked equation consistent) to discretize and solve the governing partial differential equations. The continuity equation is utilized to update the pressure field. An algebraic multigrid method (AMG) is used to speed up convergence for the iteration. All studies in this paper employ

Fig. 2 Micro-pumps with n pumping chambers in **a** series configuration with phase difference $\Delta\phi$ between neighboring chambers and **b** top view of basic configuration of the $n = 3$ peristaltic micropump, chamber length and width D, connecting channel length c, connecting channel width cw, ending channel length e and ending channel width ew
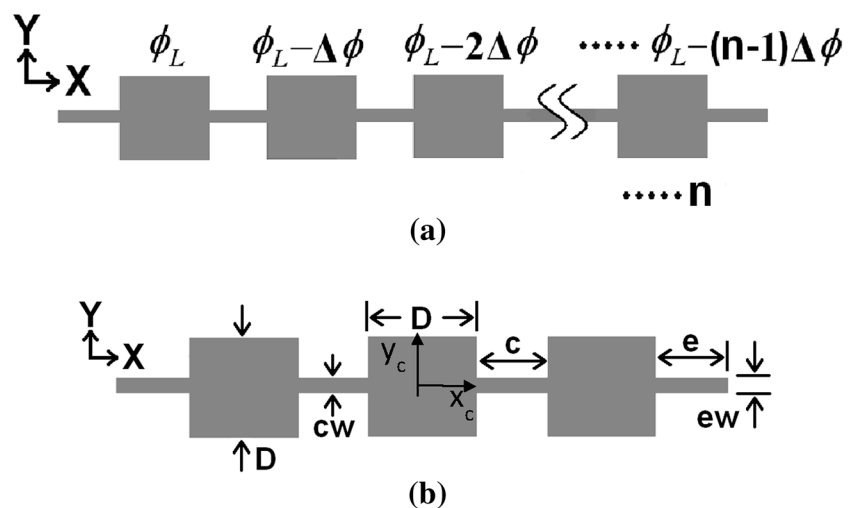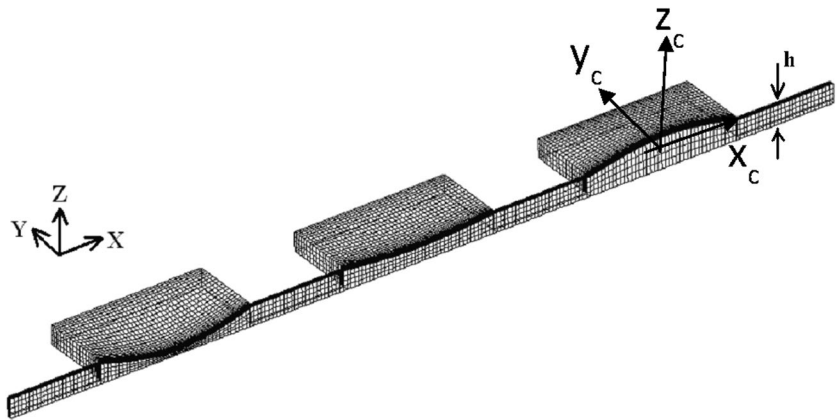
structured multizone grid, second order upwind difference for the spatial discretization, and an implicit method with blending factor $\beta = 0.6$ for the time integration. When $\beta = 0.5$, the time integration is the second-order accurate Crank–Nicolson method. When $\beta = 1$, it is the first order Euler implicit method. In this paper $\beta = 0.6$ is used because of the compromise between time accuracy and numerical stability. The time step size used in unsteady computations is chosen such that the period of the pump diaphragm oscillation will take 100 time steps to complete. The convergence criterion for the residuals in all variables is 1×10^{-6}.

2.1.1 Basic pump configuration and computational grid

Figure 2b shows the top view of the basic configuration of a peristaltic micropump with three ($n = 3$) pumping chambers. The top wall of the pumping chamber is the pumping diaphragm that drives the fluid flow. In this investigation the pumping chamber in its neutral position is a square shaped cavity of width D and depth h. The chambers are connected by micro-channels with rectangular cross-sectional area of depth h and width cw or ew. Note that the cavity height is the same as the channel height. The channel length between chambers is c, and the channel length of the leftmost and the rightmost section is e. Although these geometric parameters can be set in numerous combinations, but in this investigation the basic configuration is assumed as $D = 1$ cm, $h = 0.01$ cm ($=100$ μm), $c = 0.5$ cm, $cw = 0.1$ cm, $e = 1$ cm, and $ew = 0.1$ cm.

The working fluid in this study is water at room temperature. It is assumed that the pump works in laminar flow regime of low Reynolds number based on the average inlet velocity and the channel height. Since the flow field is symmetric with respect to the middle plane of the channel and the pumping chamber, the computational domain can be reduced by half, taking advantage of the symmetry plane. Figure 3 shows the computational grid with

symmetry plane as a grid boundary surface. In this figure, the displacement of the top wall of the chamber diaphragm is also indicated. This grid is constructed using multizone strategy. Each chamber and each microchannel section separated by the chamber is a grid zone by itself, adding up to a total of 7 grid zones for this basic configuration. Before the numerical simulation, grid dependence test is validated by using the experiments of Akhavan et al. (1999). In the experiment, a piston at the inlet end of a 3D circular pipe oscillates harmonically to drive the flow in the pipe, and the velocity profile at the mid section of the pipe is measured. The diameter of the pipe is R. The Stokes layer thickness δ is defined as $\delta = \sqrt{\omega/2\nu}$ where ω is the angular frequency of the piston oscillation, ν is kinematic viscosity of the working fluid. The case studied in this thesis has a Stokes parameter $\Lambda = R/\delta = 3.6$ and a Reynolds number $\mathrm{Re} = U\delta/\nu = 233$ where the axial velocity at the inlet due to piston oscillation is $u = U\sin(\omega t)$. The length and radius of this circular pipe are respectively 8000 and 10 mm. In our computation, the computational domain is reduced to 2D section along the axisymmetric line, and grid size is 2001×26. The upper boundary is a viscous wall, the left boundary is a moving wall oscillating at an axial velocity $u = U\sin(\omega t)$. The right boundary is an open end with a constant atmospheric pressure of 1 atm. The bottom boundary is the axis of axisymmetry. The computation employs the second order upwind difference for the spatial discretization and an implicit method with blending factor $\beta = 0.6$ for the time integration. The time step size for time integration is chosen such that one period of the oscillating wall takes 360 time steps to complete. After the tenth cycles of the wall oscillation, the computational velocity profiles along radial direction r/R at the mid-section of the pipe are compared with the experimental results. This validation case has basically confirmed that the CFDRC is capable of the calculating the pipe flow with an oscillating wall at one end of low frequency. According to grid independent test results, the number of grid points

for this basic configuration (Fig. 3) in length, width and depth is 25 × 40 × 40 for the chamber, 15 × 20 × 40 for the microchannel between chambers and 25 × 20 × 40 for the leftmost and the rightmost microchannel section. The total number of grid points in this 7-zone grid is 1,84,000. When the micropump configuration is changed by adding more chambers or by modifying the microchannel geometry, more grid zones with increased or decreased number of grids will be used accordingly.

2.1.2 Boundary conditions

The leftmost and the rightmost ends of the grid are the inlet or the outlet of the pump depending on the flow direction. The pressure at these end planes are set to a constant atmospheric pressure of 1 atm. The velocities at these planes are obtained by extrapolation satisfying the mass conservation and total pressure and total temperature relations. All viscous wall satisfy no-slip condition, hence the flow velocity at the wall equals to the velocity of the wall. The oscillating diaphragms are treated by using moving wall boundary conditions. The oscillation mode is described in next section. The initial condition is a static flow in all studies.

2.1.3 Diaphragm oscillation

The top wall of the chamber plays the role of oscillating diaphragm that drives the flow. As the top wall moves in a preset motion, the grid in the chamber also moves accordingly. The movement of the grid is handled by the grid-deformation module of CFD-ACE+ automatically. In this investigation, the diaphragm is preset to a simple harmonic motion with a local coordinate (x_c, y_c, z_c) of the diaphragm. For a diaphragm whose equilibrium position is on the x_c–y_c plane of $z_c = 0$, the displacement of the oscillating diaphragm in the z_c-direction is given by:

$$z_m(x_c, y_c, t) = A \times \sin\left(\frac{\pi x_c}{D}\right) \times \sin\left(\frac{\pi y_c}{D}\right) \times \cos\left(\omega t + \varphi\right) \quad (2c)$$

where $z_m(x_c, y_c, t)$ is the displacement of the membrane, A is amplitude of the displacement, D is the width of the pumping chamber, ω is the angular frequency, φ is a phase angle. Equation (2c) describes a sinusoidal unimodal surface oscillating up and down in z_c-direction at an angular frequency ω. This surface shape is only an approximation of the actual mode shape of a vibrating diaphragm. It is used here for simplicity based on the assumption that the mode shape effect is independent of the phase effect. In this study, the amplitude A is set to equal to chamber depth h such that $A/h = 1$. The maximum velocity of the oscillating diaphragm can be derived from Eq. (2c), and it is used as the reference velocity U_{ref} to define Reynolds number. The depth of the micro-channel is used as the reference length

L_{ref}. When the frequency f is 1 Hz and the working fluid is water at 25 °C, the Reynolds number $\frac{U_{ref} L_{ref}}{(\mu/\rho)}$ is 0.063. This Reynolds number is small and in the regime of laminar flow. Although frequency is an important parameter in peristaltic pump operation, it is not the focus of our investigation. Hence the working frequency for all simulations in this paper is set to $f = 1$ Hz, or $\omega = 2\pi f = 2\pi$ rad/s. It is also expected that the frequency effect is independent of the phase effect.

2.1.4 Operation of peristaltic micro-pump

The basic configuration of a peristaltic micro-pump sets the three pumping chambers in series arrangement, as shown in Fig. 2b. The oscillation motion of the each pumping chamber is defined by Eq. (2c), and the phase angle of the each chamber differs by a fixed phase difference $\Delta\varphi$. To pump flow from left to right, the phase of the chamber on the right should have a phase lag with respect to the chamber on the left. Let the phase angle of the first chamber from the left be φ_L. The phase angle of the second chamber lagging behind is $\varphi_L - \Delta\varphi$ where $\Delta\varphi$ is a positive number. The phase angle of the third chamber is $\varphi_L - 2\Delta\varphi$. For the series configuration of n chambers in Fig. 2a, the leftmost chamber has a phase angle of φ_L and the nth chamber from the left has a phase angle of $\varphi_L - (n-1)\Delta\varphi$. Here, each chamber works independently at a fixed phase difference $\Delta\varphi$ between two consecutive chambers.

2.1.5 Pumping flow rate, stroke volume and pumping efficiency

Generally, to obtain high pump flow rate under design constraints is an important design goal. There are numerous factors that will affect the pump flow rate, but in this investigation we are mainly interested in the relationship between the pump flow rate and oscillation phase difference $\Delta\varphi$ between consecutive chambers. The net volume flow rate of a peristaltic pump in one period (T) of oscillation can be obtained by computing the net volume V_T passing through the rightmost end plane of the channel as

$$V_T = \int_0^T \left(\int_{A_{end}} \vec{v}_{end} \cdot d\vec{A} \right) dt \quad (2d)$$

where $\vec{v}_{end}$ is the velocity on the end plane, $\vec{A}_{end}$ is the surface area of the end plane, positive when pointing outward. The average pump volume flow rate in one period is $Q_T = \frac{V_T}{T}$.

The stroke volume of a chamber diaphragm is defined as the maximum change of chamber volume in one period of diaphragm oscillation. Figure 1 shows the stroke volume definition in 2D case. When the diaphragm displacement

in 2D is derived by Eq. (2c), the stroke volume can be obtained as

$$V_{stroke} = 2 \int_0^D \int_0^D A \sin\left(\frac{\pi x_c}{D}\right) \sin\left(\frac{\pi y_c}{D}\right) dx_c dy_c$$
$$= 8A\left(\frac{D}{\pi}\right)^2 \tag{2e}$$

for a square diaphragm with $0 \leq x_c, y_c \leq D$.

In a regular pump equipped with perfect check valves, this change in chamber volume can be transformed completely into volume flow in the direction permitted by the check valve. In this ideal situation the volume flow rate generated by one pumping chamber would be $Q_s = V_{stroke}/T$. For a pump with n pumping chambers, the theoretical maximum volume flow rate obtainable is then $Q_{ideal} = (nV_{stroke})/T$.

For a peristaltic pump, there is no check valve employed in the design, and Q_{ideal} represents the ideal flow rate of a perfect peristaltic pump design. Hence, we define the pumping efficiency η of a peristaltic pump as

$$\eta = \frac{Q_s}{Q_{ideal}} = \frac{V_T}{nV_{stroke}} \times 100\% \tag{2f}$$

A larger η implies a better pumping efficiency and hence is desirable. Note that η is independent of oscillation frequency f, and it is mainly determined by the phase difference between chambers.

2.2 Experimental approaches

In this paper, experiments are also set up in an attempt to verify the computational findings. The proposed experiment will examine the basic 3-chamber peristaltic micropump, the 4-chamber and 5-chamber peristaltic micropumps in series configurations, as shown in Fig. 4. The numerical simulation in previous section have adopted rectangular chamber shape for its ease in grid generation. In experiments, circular shaped chamber is to be used for its ease in fabrication. It is speculated that although different diaphragm shape will produce different pump flow rate due to the difference in stroke volume, but at low frequency the diaphragm shape should have no effect on the relationship between phase difference and the pump flow rate.

The diameter D of the circular diaphragm is set to 1 cm, which is the same as the side length of the square diaphragm used in numerical simulation. Other geometric parameters in the basic parameter set remain unchanged, namely, $c = 0.5$ cm, $cw = 0.1$ cm, $e = 1$ cm, $ew = 0.1$ cm, and $Pe = 0.5$ cm. As for the depth of the microchannel and the pump chamber, it is set to $h = 0.05$ cm (500 μm) in order to obtain high pump flow rate. The magnetic actuation method similar to the research studies (Pan et al. 2004; Shen and Gijs 2009; Shen et al. 2011) is employed here. The pumping diaphragm is fabricated using PDMS with iron-particle contents. It will be attracted and deformed

Fig. 4 Schematic diagram of experimental peristaltic micropumps a 3-chamber configuration, b 4-chamber series configuration, c 5-chamber series configuration
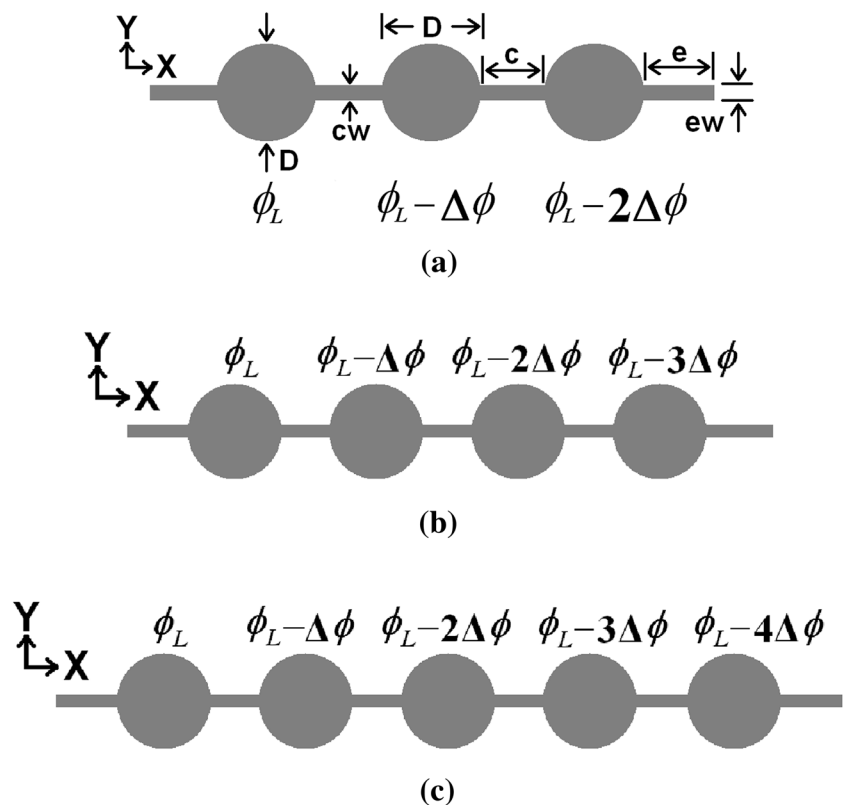
when a permanent magnet is nearby, and it will restore to its natural position as the magnet is away. In the paper of Pan et al. (2004), the phase difference between pumping chambers is fixed at 120°. In this study, the permanent magnets are driven by three rotary cams so designed that the phase difference between the magnetic forces attracting the diaphragm can be varied between 10° to 120°. For simplicity, the waveform of the magnetic force experienced by the diaphragm against time is a near square wave of a duty ratio 1/2 with steep ascending and descending rates.

2.2.1 Fabrication of peristaltic micropump

A composite material of PDMS mixture (Polydimethylsiloxane, Sylgard 184 silicone elastomer, Dow Conring Corporation) and iron particles (10 µm diameter of a particle, Merck Chemicals Corporation) is used to construct the pumping diaphragm. The composite material is named as "Fe-PDMS". The preparation for Fe-PDMS is described in the references (Nagel et al. 2006; Jiang 2009; Leu and Jiang 2010) and the thickness of Fe-PDMS diaphragm in experiments is also discussed in the thesis of Jiang (2009). The difference in material characteristics, such as elasticity and hydrophobicity, between Fe-PDMS and general PDMS is insignificant, but the iron particles in Fe-PDMS make it be actuated by external magnetic fields. The fabrication processes of a 3-chamber peristaltic micropump are illustrated in Fig. 5, and listed below:

1. A 4″ diameter silicon wafer is cleaned first. Then the silicon wafer is coated with a thick film of SU-8-50 photoresist (MicroChem Corporation) using spin coating process. The coated film thickness is 500 µm. It is obtained by an adequate amount of the photoresist SU-8 spreading on the silicon wafer, which is spun at 100 rpm for 120 s by a spin coater. The film coating is then subjected to a soft bake at 95 °C for 4 h to establish its photoresist characteristics. The spin coating and the soft bake process are illustrated in Fig. 5a.

2. The film of SU-8-50 is exposed to UV light with a designed mask on its top. The transparent part of the mask allows UV light to go through during exposure. The masked part of the mask blocks UV light from the photoresist during exposure. Then, a post-exposure bake at 65 °C for 30 min is performed after the exposure process. These processes are illustrated in Fig. 5b, c.

3. The development process in Fig. 5d is executed after the post-exposure bake. Because SU-8 photoresist is a negative photoresist, the unexposed photoresist will be removed by the PGMEA (propylene glycol monomethyl ether acetate) developer during development. The exposed SU-8 photoresist will remain on the silicon wafer after development. Then, the remaining photoresist is subjected to a hard bake process at 95 °C for 10 min to produce a SU-8 master mold on the silicon wafer.

4. The PDMS mixture is prepared at a ratio of 10 parts silicone base to one part curing agent by weight. The Fe-PDMS mixtures are also prepared at a ratio of 3 parts iron particles to one part PDMS base by weight. The PDMS mixture is then poured into the SU-8 master mold in which it is cured at 95 °C for 40 min on the hotplate. The microchannel part on the master mode is covered with the PDMS mixture, but the chamber part is not. After the PDMS mixtures are cured, Fe-PDMS mixtures are poured into the chamber part of the master mold. To control a Fe-PDMS film of thickness 0.03 cm (300 µm) which is demonstrated in the thesis of Jiang (2009) that Fe-PDMS diaphragm for this thickness can be substantially deformed at frequency 1 Hz, Fe-PDMS is spun at 300 rpm for 60 s by a spin coater. Fe-PDMS mixtures on the master mold are cured at 95 °C for 40 min on the hotplate. Finally, the membrane layer consisting of PDMS and Fe-PDMS mixtures is peeled off from the master mold. These processes are illustrated in Fig. 5e, f.

5. Two holes are machined on the membrane layer for the inlet and outlet of the micropumps. Then oxygen plasma is used to bond PDMS and Fe-PDMS membrane to a glass plate of 2 mm thickness. It is cured at 100 °C for 20 min to finalize the micropump configuration. The bonding process is illustrated in Fig. 5(g). Finally, the two ends of the bottom of the peristaltic micropump is adhered to two aluminum frames (dimensions: length 30 cm, width 0.8 cm, and depth 0.8 cm) by super glues, as shown in Fig. 6. The peristaltic micropump can be fastened on two support jacks by aluminum frames and C-clamps.

2.2.2 Experimental setup

The schematic experimental setup and photo is shown in Figs. 7, 8a. The magnet support, the rotary cams and the linkage mechanisms are shown in Fig. 8b. In rotary cam design, the cam shaft with three to five cam disks is driven by a motor (Brushless motor BLH230K-30, Oriental Motor Company Limited), and the rotational speed is set to 60 rpm ($f = 1$ Hz). The circumferential contour of the cam disk is in contact with the contact wheel at the bottom end of the magnet frame having two permanent magnets attached to the horizontal arms as shown in Fig. 8b. As the cam disk rotates the magnets will move up and down following the variation in the cam contour. By designing contours of rotating cam discs, the magnets will move up and down with vertical displacement curve. To accurately adjust phase difference between two rotating cam discs, a

Fig. 5 Schematic diagram of fabrication processes of micropumps. **a** Spin coating with SU-8 50 photoresist and soft bake process, **b** exposure process, **c** post-exposure bake process, **d** development process and hard bake process, **e** replica molding with PDMS and Fe-DPMS mixtures, **f** replica stripping, **g** bonding PDMS to glass base by oxygen plasma

(a)

(b)

(c)

(d)

(e)

(f)

(g)
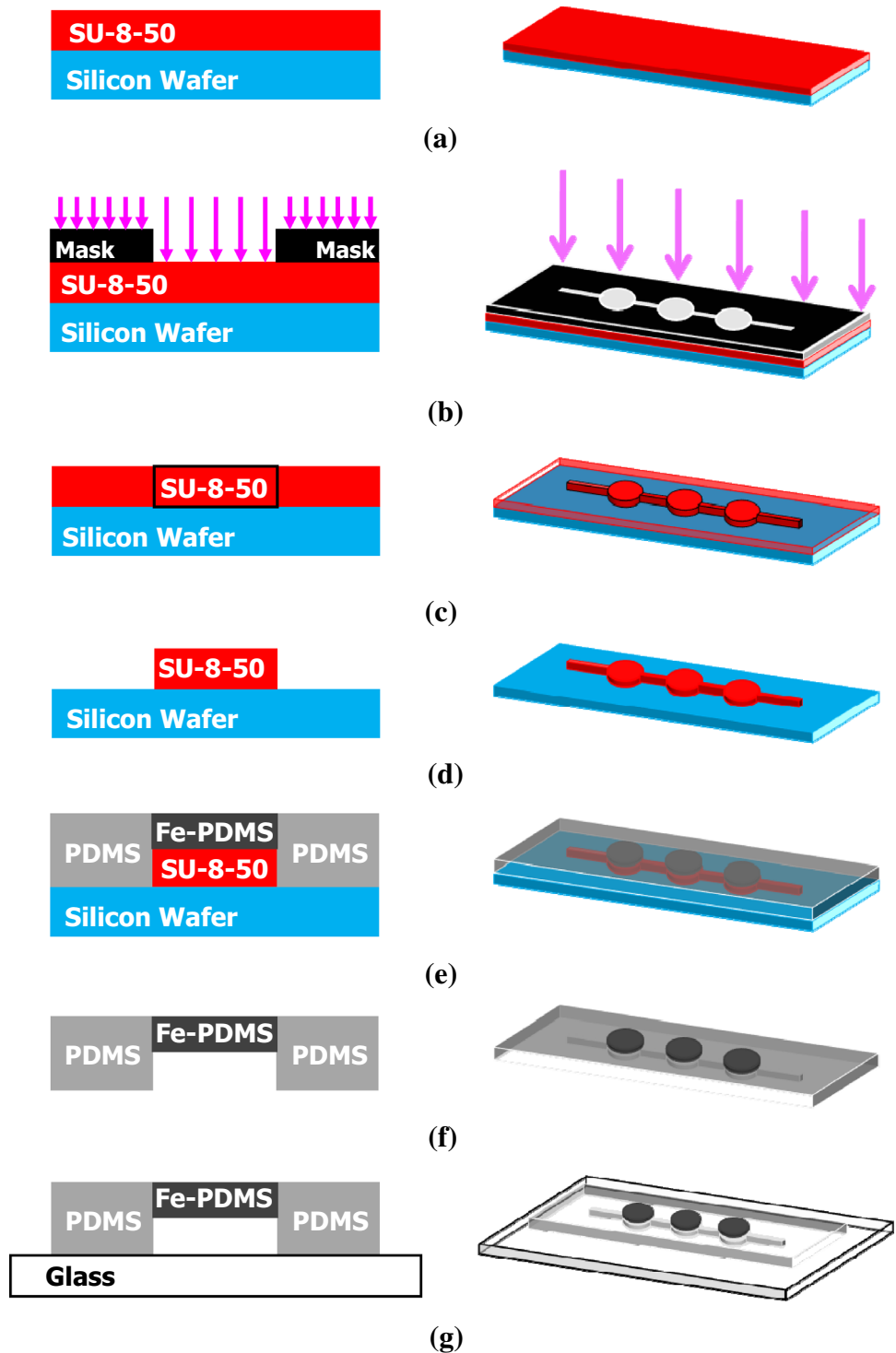
set of holes are fabricated on the discs, as shown in Fig. 8b. These holes are so arranged that the angular position of the cam disc relative to each other can be fixed by inserting four hinge pins into corresponding holes. As the cam shaft rotates, the displacement history of the magnet frame above the cam disk will have a phase difference between two neighboring magnet frames. Note that the phase difference is measured relative the rightmost cam disc rotating in clockwise direction such that each cam is lagging behind the cam on its right a fixed phase difference $\Delta\varphi$. The micropump fastened to the aluminum frames is fixed on support jacks. It is placed in the center of the hollow zone of the magnet frame such that one magnet is above the pump chamber and the other magnet is below the pump chamber.
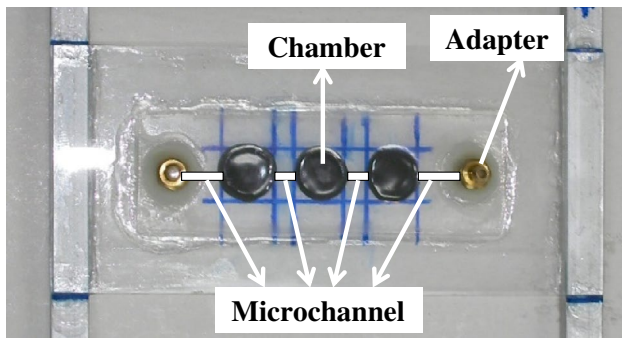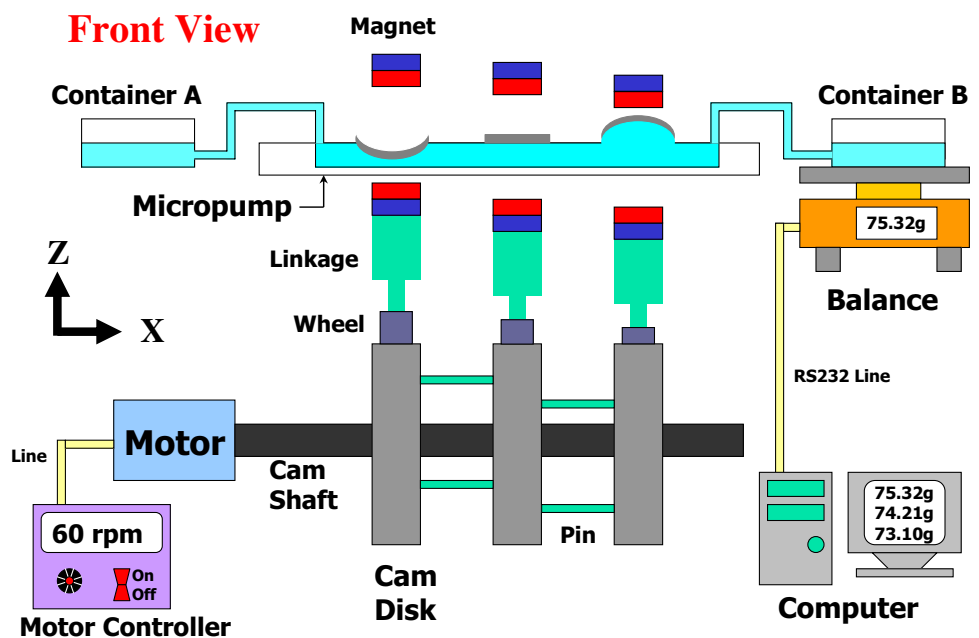
Fig. 6 Finished micropump fastened on two support aluminum frames (dimensions: length 30 cm, width 0.8 cm, and depth 0.8 cm) by super glues

These magnets are aligned and positioned in line with the pump chamber. The magnets will attract the Fe-PDMS diaphragm and force the diaphragm to move up and down, as the magnet frame moves up and down following the cam disk's rotation. The diaphragm movement will drive the fluid flow in and out of the chamber. The phase of the diaphragm motion can be controlled by adjusting the rotary cam positions. There are two reservoirs connected to the micropump by silicon tubes, one at inlet and the other at outlet. The container at outlet is placed on a precision balance (BJ410C, capacity 400 ± 0.01 g, Precisa Gravimetrics AG). A RS232 to RJ45 line transmits the balance reading to the PC computer, and the data from the balance is immediately recorded and analyzed by a program BALINT (version: 5.0, Precisa Gravimetrics AG) running on personal computer.

To test the repeatability of the experimental results, three separate "complete set of experiments" are performed at different times of a day for each pump configuration. The test results found that the relation between pump flow rate and phase difference is similar. The three sets of experiment are almost parallel to each other. The deviation from the mean pump flow is less than 7 % for phase differences between 20° and 80°, although it can be as high as 31 % at a phase difference of 10°. Nonetheless, the repeatability test results conclude that the relation between pump flow rate and the phase difference has a good repeatability using the experimental setup in this paper.

3 Numerical and experimental results

3.1 Numerical simulation results of pump flow rate and phase difference in series configuration

In this section, the computational results for peristaltic pumps with pumping chamber in series operation are presented. The main purpose is to investigation the effects of phase difference $\Delta\varphi$ on the pump flow rate in these pumps. Other geometric parameters are all fixed at the same value as the basic 3-chamber configuration. That is, $D = 1$ cm, $c = 0.5$ cm, $cw = 0.1$ cm, $e = 1$ cm, $ew = 0.1$ cm, $h = 0.01$ cm and $A = h$. The membrane oscillation frequency is kept at $f = 1$ Hz or $\omega = 2\pi$ (rad/s).

The computations are done for the cases with $\Delta\varphi$ varying from $\Delta\varphi = 10°$ to $\Delta\varphi = 120°$ and the number of pumping membrane varying from $n = 3$ to $n = 8$. The pump flow rates are obtained and plotted in Fig. 9. The corresponding

Fig. 7 Schematic diagram of experimental setup

(a)

(b)
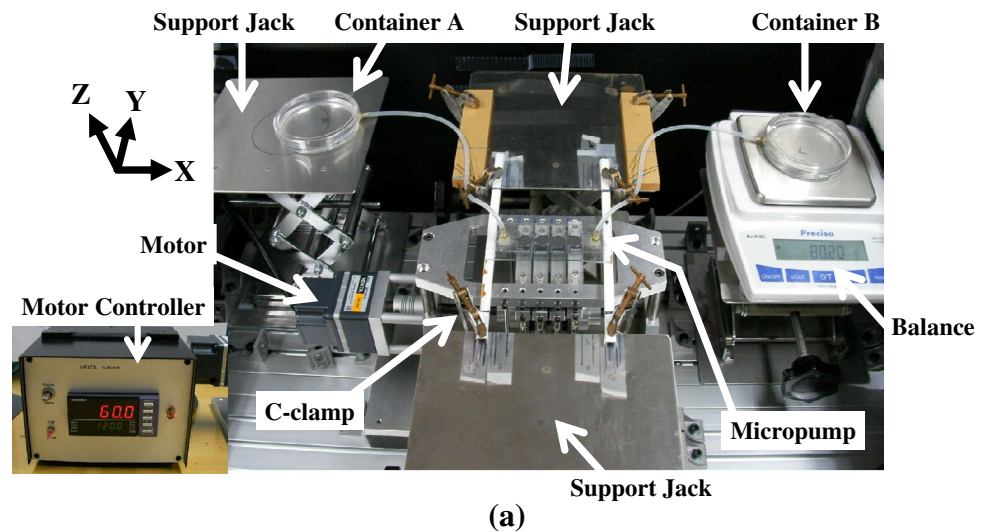
pumping efficiencies are plotted in Fig. 10. In these figures, different symbols represent different number of pumping chamber in the configuration. For each n, there is a phase difference angle $\Delta\varphi_{max}$ corresponding to the maximum flow rate Q_{max} and the maximum pumping efficiency η_{max} is obtained.

When the number of pump chamber is increased from $n = 3$ to $n = 8$ in series configuration, the maximum phase difference $\Delta\varphi_{max}$ decreases monotonically from $\Delta\varphi_{max} = 64.5°$ to $\Delta\varphi_{max} = 26.9°$; the maximum pump flow rate Q_{max} increase monotonically from $Q_{max} = 99.6$–349.6 μL/min; and the maximum pumping efficiency η_{max} increase monotonically from $\eta_{max} = 6.8$ % to $\eta_{max} = 8.9$ %. From Fig. 9, one can see that the influence of phase difference $\Delta\varphi$ on pump flow rate becomes more and more significant when n is increased. For example, for a basic 3-chamber peristaltic micropump, when the phase difference is at a non-optimal angle, say $\Delta\varphi = 90°$, the pump flow rate is about $Q \cong 85$ μL/min, which is not very far

from the $Q_{max} = 99.6$ μL/min at $\Delta\varphi_{max} = 64.5°$. But for an 8-chamber series configuration, the pump flow rate at $\Delta\varphi = 90°$ is about $Q \cong 105$ μL/min as compared with the $Q_{max} = 349.6$ μL/min at $\Delta\varphi_{max} = 26.9°$. This has clearly demonstrated the importance of operating at the correct $\Delta\varphi_{max}$ when n is increased in a series configuration.

Note that the increase in Q_{max} as n is increased by one is about 50 μL/min for all configurations. This implies that the increase in the maximum efficiency η_{max} will be gradually decreased with increasing n, because the total stroke volume is proportional to n. This can be seen from the plot of pumping efficiency at various phase differences in Fig. 10. The maximum efficiency η_{max} in all cases is less than 9 %. This low pumping efficiency for peristaltic pump is not really surprising, since there is no check valve employed in the pump configuration. Note that the importance of operating at $\Delta\varphi_{max}$ phase difference is very clear in terms of pumping efficiency. For example, when a fixed $\Delta\varphi = 90°$, the
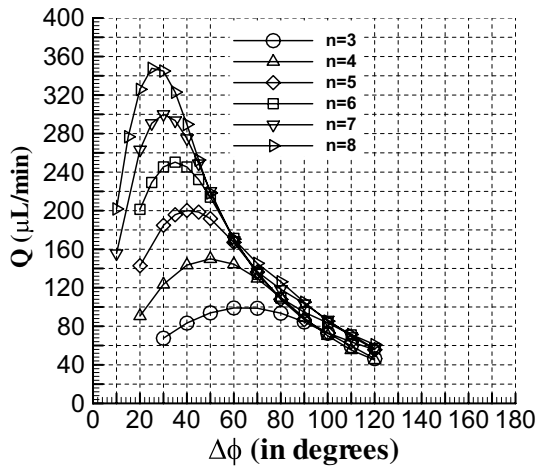
Fig. 9 Computed pump flow rate Q versus phase difference $\Delta\phi$ for series micropumps with number of chambers from $n = 3$ to $n = 8$, geometric parameter set: ($D = 1$ cm, $c = 0.5$ cm, $cw = 0.1$ cm, $e = 1$ cm, $ew = 0.1$ cm, and $A = h = 0.01$ cm)
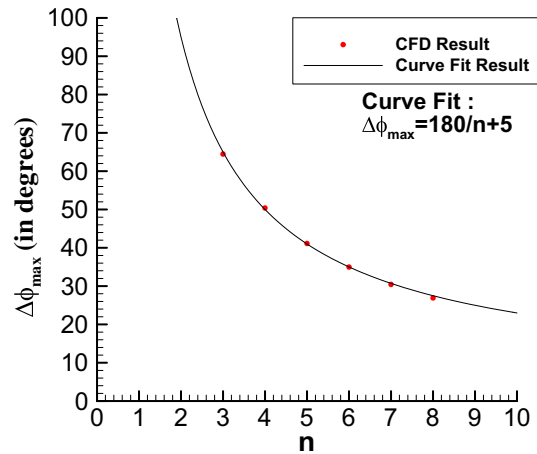

Fig. 11 Simple rule between the maximum phase difference $\Delta\phi_{max}$ at which Q_{max} occurs and the curve fitting line by Eq. (2g)
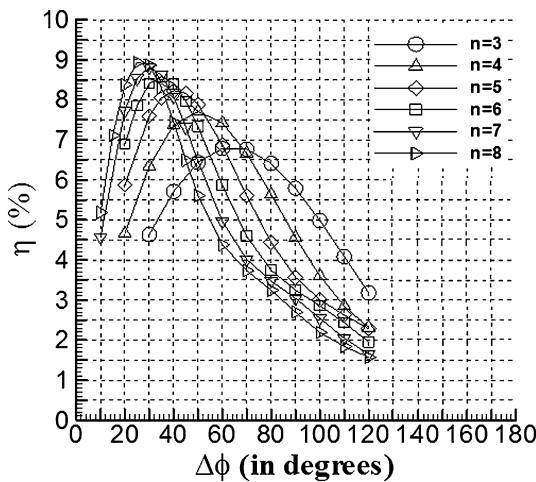

Fig. 10 Computed pumping efficiency η versus phase difference $\Delta\phi$ for series micropumps with number of chambers from $n = 3$ to $n = 8$, geometric parameter set: ($D = 1$ cm, $c = 0.5$ cm, $cw = 0.1$ cm, $e = 1$ cm, $ew = 0.1$ cm, and $A = h = 0.01$ cm)
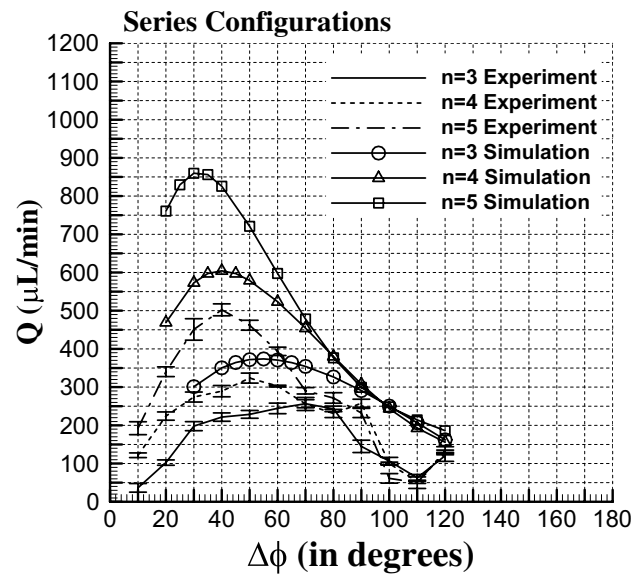

Fig. 12 Comparisons between computational and experimental pump flow rates for series micropumps, diaphragm amplitude: $A = h = 0.05$ cm, *circle* computation and 3-chamber, *triangle* computation and 4-chamber, *square* computation and 5-chamber, *solid line* experiment and 3-chamber, *dash line* experiment and 4-chamber, *dash-dot line* experiment and 5-chamber

pumping efficiency η actually decreases as the number of pumping chamber increases from $n = 3$ to $n = 8$.

The simple rule between the maximum phase difference and the number of the pumping chamber is discovered as following below:

$$\Delta\varphi_{max} = \frac{180°}{n} + const, \ 3 \leq n \leq 8 \qquad (2g)$$

where $\Delta\varphi_{max}$ is the maximum phase difference at which Q_{max} occurs, n is the number of pumping chamber, const is a constant. Here, const $= 5°$ is based on the geometric parameters of the basic configuration of the micropump in

this paper. Figure 11 shows that the computational results are in agreement with the results of Eq. (2g).

3.2 Experimental results and discussion

3.2.1 Pump flow rate versus phase difference in series configuration

In this section, experimental results are demonstrated for 3-chamber, 4-chamber and 5-chamber peristaltic

micropump in series configuration. The phase difference between two neighboring chambers is varied from 10° to 120° in 10° increment. The measured pump flow rate, as well as the computational results with an amplitude $A = h = 0.05$ cm, for $n = 3$ to 5, is shown in Fig. 12. In Fig. 12, the uncertainty is less than 7 % for phase difference between 20° and 80°. Most high uncertainty cases occur for phase difference of 10° or greater than 90°. All three curves are convex in the middle portion with a global maximum flow rate Q_{max} occurring at a specific phase difference $\Delta\phi_{max}$. It is seen that $\Delta\phi_{max}$ decreases with increasing n, which follows the same trend predicted by the computational results Fig. 11. The influence of phase difference becomes more significant as the number of pumping chamber increases. For example, when comparing with the pump flow at $\Delta\phi = 100°$, we have for $n = 3$, pump flow rate increases from 106.47 µL/min to its $Q_{max} = 256.58$ µL/min at $\Delta\phi_{max} = 70°$; for $n = 4$, pump flow rate increases from 100.03 µL/min to its $Q_{max} = 323.7$ µL/min at $\Delta\phi_{max} = 50°$; while for $n = 5$, pump flow rate increases from 61.21 µL/min to its $Q_{max} = 502.31$ µL/min at $\Delta\phi_{max} = 40°$. Note that it is important to operate at $\Delta\phi_{max}$ in order to obtain the maximum pump flow rate. For example, if we operate 5-chamber pump at $\Delta\phi = 70°$ (which is the $\Delta\phi_{max}$ for a 3-chamber pump), then the pump flow is only 290.38 µL/min as compared with the achievable $Q_{max} = 502.3$ µL/min.

All there curves in Fig. 12 have a local minimum at $\Delta\phi = 110°$. No explanation has been found for this behavior. Even at $\Delta\phi = 100°$, or 120° the pump flow rates do not change much as the number of pumping chamber increases from $n = 3$ to $n = 5$. This implies that the phase difference around 110° should be avoided in the operation of series pumps. One can compare the three experimental curves with the computational results in Fig. 12. It can be clearly seen that the trend of decreasing $\Delta\phi_{max}$ with increasing n is the same for experimental data and computational data. The numerical values are different in magnitude mainly because of (1) different chamber shape, (2) different channel length and shape, and (3) different wave form of diaphragm movement. In particular, the wave form in experiment is a near square wave with a duty ratio ~0.5, while in computation the wave form is sinusoidal with a duty ratio = 0.5.

4 Conclusion

In this work, phase difference effects on the flow rate of peristaltic micropumps are studied using computational fluid dynamics simulation and experimental validation. The basic configuration of peristaltic micropumps consists of three pumping chambers operating in a particular peristaltic sequence to drive the fluid flow in micro-channels.

In the past, many researches have worked on the relations between pump flow rate and factors such as pumping frequency, diaphragm amplitude, geometric parameters of the pumping chambers and microchannels etc., under the operation of a chosen peristaltic sequence of diaphragm actuation. The chosen peristaltic sequence basically determines the phase relation between neighboring pumping chambers. For example, the common phase difference between chambers is 60° for a 6-step peristaltic sequence (Jang et al. 2009; Graf and Bowser 2008; Shen and Gijs 2009; Shen et al. 2011), 90° for a 4-step peristaltic sequence (Jang et al. 2007; Graf and Bowser 2008; Jang and Yu 2008; Nguyen et al. 2008; Jang et al. 2009) and 120° for a 3-step peristaltic sequence (Jang et al. 2007; Jang and Yu 2008; Lin et al. 2007; Xie et al. 2004). Very few research works have examined the phase difference effect on peristaltic micro-pump.

In this work, we concentrate on the phase difference effects by fixing the chamber and microchannel geometry at their typical values. The depth of the chamber and microchannel is set to $h = 0.01$ cm. The wave form of the diaphragm movement is set to a harmonic oscillation for its ease in grid generation. The oscillation frequency is set to $f = 1$ Hz, and the amplitude is $A = h$. To pump flow toward right, the chamber on the right should have a phase lag $\Delta\phi$ behind the chamber on the left. The phase difference ranging from 30° to 120° is studied. For the 3-chamber basic configuration, the maximum pump flow $Q_{max} = 99.6$ µL/min occurs at $\Delta\phi_{max} = 64.5°$ (maximum phase difference). Considering the situation that more pumping chambers could be added in order to derive more pump flow, the number of pumping chamber n is varied in the computation from 3 to 8 in series configurations. It is found that, for series configurations, the maximum flow rate Q_{max} increases with increasing n to $Q_{max} = 349.6$ µL/min for $n = 8$, while the phase difference at which Q_{max} occurs drops with increasing n to $\Delta\phi_{max} = 26.9°$ for $n = 8$. The results indicate that it is extremely important to work at the appropriate phase difference, for otherwise, the pumping efficiency will drop instead of increase with increasing n. It also clearly validate that the trend of decreasing $\Delta\phi_{max}$ with increasing n is the same for experimental data and computational data.

References

Akhavan R, Kammz RD, Shapiro AH (1999) An investigation of transition to turbulence in bounded oscillatory stokes flows part 1. Experiments. J Fluid Mech 225:395–422

Boden R, Hjort K, Schweitz JA, Simu U (2008) A metallic micropump for high-pressure microfluidics. J Micromech Microeng 18(11):115009-1–115009-7

Du M, Ye X, Wu K, Zhou Z (2009) A peristaltic micro pump driven by a rotating motor with magnetically attracted steel balls. Sensors 9(4):2611–2620

Graf NJ, Bowser MT (2008) A soft-polymer piezoelectric bimorph cantilever-actuated peristaltic micropump. Lab Chip 8(10):1664–1670

Grosjean C, Tai YC (1999) A thermopneumatic peristaltic micropump. In: Proceedings of Transducers' 99, Sendai, Japan, pp 1776–1779

Huang SB, Wu MH, Cui ZF, Cui Z, Lee GB (2008) A membrane-based serpentine-shape pneumatic micropump with pumping performance modulated by fluidic resistance. J Micromech Microeng 18(4):045008-1–045008-12

Jang LS, Yu YC (2008) Peristaltic micropump system with piezoelectric actuators. Microsyst Technol 14(2):241–248

Jang LS, Li YJ, Lin SJ, Hsu YC, Yao WS, Tsai MC, Hou CC (2007) A stand-alone peristaltic micropump based on piezoelectric actuation. Biomed Microdevices 9(2):185–194

Jang LS, Shu K, Yu YC, Li YJ, Chen CH (2009) Effect of actuation sequence on flow rates of peristaltic micropumps with pzt actuators. Biomed Microdevices 11(1):173–181

Jiang PC (2009) Fe-PDMS composite membrane for microfluidic chip applications. Master thesis Institute of Nanotechnology and Microsystems Engineering, National Cheng Kung University, Tainan Taiwan, ROC

Kim EG, Sim WC, Oh J, Choi B (2002) A continuous peristaltic micropump using magnetic fluid. In: 2nd annual international IEEE-EMB special topic conference on microtechnologies in medicine and biology, Madison, Wisconsin, USA, pp 509–513

Koch C, Remcho V, Ingle J (2009) PDMS and tubing-based peristaltic micropumps with direct actuation. Sens Actuators B Chem 135(2):664–670

Laser DJ, Santiago JG (2004) A review of micropumps. J Micromech Microeng 14(6):R35–R64

Leu TS, Jiang PC (2010) Fe-PDMS fabricated microchannels for peristaltic pump applications. In: Proceedings of the 5th IEEE international conference on nano/micro engineered and molecular systems, Xiamen, China, pp 646–649

Li JH, Kan WH, Jang LS, Hsu YC (2007) A portable micropump system based on piezoelectric actuation. In: The 33rd annual conference of the IEEE industrial electronics society (IECON) Taipei Taiwan, pp 2898–2903

Lin Q, Yang B, Xie J, Tai YC (2007) Dynamic simulation of a peristaltic micropump considering coupled fluid flow and structural motion. J Micromech Microeng 17(2):220–228

Lotz P, Matysek M, Schlaak HF (2009) Peristaltic pump made of dielectric elastomer actuators. In: Proceedings of SPIE, vol 7287, pp 72872D-1–72872D-8

Nagel JJ, Mikhail G, Noh H, Koo J (2006) Magnetically actuated micropumps using an Fe-PDMS composite membrane. In: Proceedings of SPIE on smart structures and materials: smart electronics, MEMS, BioMEMS, and nanotechnology, vol 6172, pp 617213-1–617213-9

Nguyen NT, Huang X, Chuan TK (2002) MEMS-micropumps: a review. J Fluids Eng 124(2):384–392

Nguyen NT, Pham M, Goo NS (2008) Development of a peristaltic micropump for bio-medical applications based on mini LIPCA. J Bionic Eng 5(2):135–141

Oh KW, Rong R, Ahn CH (2005) Miniaturization of pinch-type valves and pumps for practical micro total analysis system integration. J Micromech Microeng 15(12):2449–2455

Pan T, Kai E, Stay M, Barocas V, Ziaie B (2004) A magnetically driven PDMS peristaltic micropump. In: Proceedings of the 26th annual international conference of the IEEE EMBS, San Francisco, CA, USA, pp 2639–2642

Pilarski PM, Adamia S, Backhouse CJ (2005) An adaptable microvalving system for on-chip polymerase chain reactions. J Immunol Methods 305(1):48–58

Shen M, Gijs MAM (2009) High performance magnetic active-valve micropump. In: International conference on solid-state sensors and actuators (Transducers 2009). Denver, Colorado, USA, pp 1234–1237

Shen M, Dovat L, Gijs MAM (2011) Magnetic active-valve micropump actuated by a rotating magnetic assembly. Sens Actuators B Chem 154(1):52–58

Shoji S, Esashi M (1994) Microflow devices and systems. J Micromech Microeng 4(4):157–171

Smits JG (1990) Piezoelectric micropump with three valves working peristaltically. Sens Actuators A 21–23:203–206

Trenkle F, Haeberle S, Zengerle R (2009) Normally-closed peristaltic micropump with reusable actuator and disposable fluidic chip. Procedia Chem 1(1):1515–1518

Wang CH, Lee GB (2006) Pneumatically driven peristaltic micropumps utilizing serpentine-shape channels. J Micromech Microeng 16(2):341–348

Wu MH, Huang SB, Lee GB (2008) A high throughput microfluidic liquid pumping system based on pneumatic micropump with serpentine layout. In: The 4th Asia Pacific conference on transducers and micro/nano technologies (APCOT), Tainan, Taiwan, pp 1–4

Xie J, Shih J, Lin Q, Yang B, Tai YC (2004) Surface micromachined electrostatically actuated micro peristaltic pump. Lab Chip 4(5):495–501

Yang YJ, Liao HH (2009) Development and characterization of thermopneumatic peristaltic micropumps, J Micromech Microeng 19(2):025003-1–025003-13